


Article

Evaluation and Adjustment of Precipitable Water Vapor Products from FY-4A Using Radiosonde and GNSS Data from China

Xiangping Chen¹, Yifei Yang^{1,*}, Wen Liu^{2,*}, Changzeng Tang¹, Congcong Ling¹, Liangke Huang², Shaofeng Xie²  and Lilong Liu²

¹ Natural Resources Information Center of Guangxi Zhuang Autonomous Region, Nanning 530200, China; xpchen@gxcors.com (X.C.); tangzhangzeng@mapgx.com (C.T.)

² College of Geomatics and Geoinformation, Guilin University of Technology, Guilin 541004, China; lkhuang@glut.edu.cn (L.H.); xieshaofeng@glut.edu.cn (S.X.); lllong99@glut.edu.cn (L.L.)

* Correspondence: yifei.yang@gxcors.com (Y.Y.); 1020211832@glut.edu.cn (W.L.)

Abstract: The geostationary meteorological satellite Fengyun-4A (FY-4A) has rapidly advanced, generating abundant high spatiotemporal resolution atmospheric precipitable water vapor (PWV) products. However, remote sensing satellites are vulnerable to weather conditions, and these latest operational PWV products still require systematic validation. This study presents a comprehensive evaluation of FY-4A PWV products by separately using PWV data retrieved from radiosondes (RS) and the Global Navigation Satellite System (GNSS) from 2019 to 2022 in China and the surrounding regions. The overall results indicate a significant consistency between FY-4A PWV and RS PWV as well as GNSS PWV, with mean biases of 7.21 mm and -8.85 mm, and root mean square errors (RMSEs) of 7.03 mm and 3.76 mm, respectively. In terms of spatial variability, the significant differences in mean bias and RMSE were 6.50 mm and 2.60 mm between FY-4A PWV and RS PWV in the northern and southern subregions, respectively, and 5.36 mm and 1.73 mm between FY-4A PWV and GNSS PWV in the northwestern and southern subregions, respectively. The RMSE of FY-4A PWV generally increases with decreasing latitude, and the bias is predominantly negative, indicating an underestimation of water vapor. Regarding temporal differences, both the monthly and daily biases and RMSEs of FY-4A PWV are significantly higher in summer than in winter, with daily precision metrics in summer displaying pronounced peaks and irregular fluctuations. The classic seasonal, regional adjustment model effectively reduced FY-4A PWV deviations across all regions, especially in the NWC subregion with low water vapor distribution. In summary, the accuracy metrics of FY-4A PWV show distinct spatiotemporal variations compared to RS PWV and GNSS PWV, and these variations should be considered to fully realize the potential of multi-source water vapor applications.

Keywords: GNSS; radiosonde; FY-4A; PWV



Academic Editors: Tin Lukić, Li Li and Pengfei Xia

Received: 22 November 2024

Revised: 8 January 2025

Accepted: 14 January 2025

Published: 17 January 2025

Citation: Chen, X.; Yang, Y.; Liu, W.; Tang, C.; Ling, C.; Huang, L.; Xie, S.; Liu, L. Evaluation and Adjustment of Precipitable Water Vapor Products from FY-4A Using Radiosonde and GNSS Data from China. *Atmosphere* **2025**, *16*, 99. <https://doi.org/10.3390/atmos16010099>

Copyright: © 2025 by the authors. Licensee MDPI, Basel, Switzerland. This article is an open access article distributed under the terms and conditions of the Creative Commons Attribution (CC BY) license (<https://creativecommons.org/licenses/by/4.0/>).

1. Introduction

Water vapor plays a critical multifaceted role in the atmosphere, with its behavior and distribution significantly influencing Earth's meteorological and climatic systems. Cooling and condensation of water vapor in the atmosphere result in cloud formation and precipitation, modulating the spatial distribution of atmospheric humidity and impacting the development and evolution of meteorological phenomena across various spatiotemporal scales. Additionally, water vapor is a major error source in space geodetic systems, causing a typical path delay of up to 25 cm in the zenith direction for the Global Navigation Satellite

System (GNSS) [1–4]. Therefore, the accurate retrieval and precision assessment of different atmospheric water vapor datasets constitute a long-term essential task across various fields.

Precipitable Water Vapor (PWV), defined as the integral of water vapor within a vertical atmospheric column, quantifies the dynamically varying water vapor and is a crucial parameter for investigating various atmospheric processes [5,6]. However, early effective technologies for obtaining PWV data, such as microwave radiometers [7], ground-based hygrometers, and sun photometers, are limited by weather conditions and the spatial configuration of measurement sites [8]. The radiosonde (RS), with an inversion uncertainty for PWV ranging from 0 to 1.5 mm, is typically considered the benchmark for validating the accuracy of PWV datasets obtained from other technologies. GNSS water vapor detection technology, with its high temporal resolution and all-weather observation capabilities, can achieve PWV retrieval accuracy within 1–2 mm [9], thereby demonstrating its potential as an effective complement to radiosondes and its utility in monitoring atmospheric water vapor [10,11].

High-precision measurements of atmospheric water vapor require dense, high-resolution observational data due to its considerable spatial and temporal variability. However, in remote and complex terrains, such as marine regions and high plateaus, the sparse distribution of observational sites impairs the timeliness and quality of the data. Reanalysis datasets, e.g., the 5th generation European Centre for Medium-Range Weather Forecasts (ECMWF) Atmospheric Reanalysis (ERA5) [12], Modern-Era Retrospective analysis for Research and Applications, Version 2 (MERRA-2) [13], and China Reanalysis and Analysis Assimilation (CRAA) [14] can provide grid-based PWV data by integrating atmospheric parameters at different height layers, exhibiting advantages such as global coverage, spatial completeness, and consistent records. However, the accuracy of water vapor products in reanalysis models may be unreliable due to the lack of or limited observational data being assimilated in certain regions [15]. Currently, multiple satellites have deployed radiometers to sense water vapor content, providing numerous datasets for assimilation into numerical weather prediction (NWP) models, effectively mitigating the deficiency of in situ sites over the ocean and becoming the primary method for retrieving water vapor in these regions [16,17]. Meteorological remote sensing satellites, e.g., Moderate Resolution Imaging Spectroradiometer (MODIS) and Fengyun, can provide large-scale PWV data [18–20], but they are constrained by cloud contamination and the limitation of data collection only during satellite overpasses, leading to temporal continuity and accuracy that are significantly inferior to those of ground-based techniques [21]. Therefore, it is essential to comprehensively validate the water vapor products from satellite observations before applying them to various analyses.

The Fengyun-4A (FY-4A) satellite, equipped with the Advanced Geostationary Radiation Imager (AGRI), represents the latest generation of Chinese geostationary meteorological satellites designed for weather monitoring, early warning and forecasting [22–24]. AGRI is capable of rapid minute-level scanning across the Asia-Pacific region [25], providing high spectral and temporal resolution atmospheric parameters essential for accurate climate and weather applications [26]. Wang et al. [27] utilized RS PWV data to evaluate FY-4A PWV products from 18 January 2019, to 18 January 2020, demonstrating that the FY-4A PWV products exhibit good consistency with radiosonde data. Tan et al. [28] evaluated one year of Fengyun PWV data from January 2019 to January 2020 using RS PWV, GNSS PWV, and ERA5 PWV, demonstrating good consistency and accuracy with RS PWV and GNSS PWV but significant discrepancies with ERA5 PWV. Zhou et al. [29] statistically evaluated the overall performance of FY-4A PWV products using PWV data from 23 GNSS stations in mainland China in 2021. Liu et al. [30] used GNSS PWV data from March 2019 to February 2020 to verify FY-4A PWV in mainland China on a regional basis.

To the best of our knowledge, few studies have examined the accuracy and applicability of FY-4A PWV products, especially comprehensive accuracy assessments over China using long-term time series and numerous diverse datasets. Therefore, the primary objective of this study is to evaluate the accuracy of FY-4A PWV using multi-source water vapor datasets from 2019 to 2022 in order to assess its performance across various temporal and spatial scales by dividing China and its surrounding regions into multiple subregions. The paper is structured as follows: Section 2 describes the datasets and methodology after this Introduction. The evaluation and analysis of FY-4A PWV between RS PWV and GNSS PWV are in Section 3. Finally, the Conclusions are in Section 4.

2. Datasets and Methods

The research area of this study encompasses China and the surrounding regions, which feature a variable geographical setting and a complex climate system, thereby influencing the distribution and movement of water vapor [31]. To facilitate the discussion on spatiotemporal PWV variability, the research area was divided into four subregions, i.e., North China (NC), Northwest China (NWC), Tibet Plateau (TP), and South China (SC). To examine PWV variability across different time scales, we categorize the months as follows: March to May for spring, June to August for summer, September to November for autumn, and December to February for winter.

2.1. RS PWV

The RS-inverted PWV is one of the most common references for measuring various high-quality water vapor data [32]. The RS profiles contain the meteorological parameters in vertical direction collected by radiosonde balloons at UTC 00:00 and UTC 12:00 every day, including surface temperature T_s , pressure P , relative humidity (RH) and geopotential height (H), etc. In this study, the meteorological parameters of RS will be used to integrate RS PWV as a reference value for evaluating the FY-4A PWV.

$$PWV = -\frac{1}{g} \int_{P_i}^{P_{i+1}} q \, dP = -\frac{1}{g} \sum_{P_i}^{P_{i+1}} q \cdot P, \quad (1)$$

$$e = \frac{RH \cdot e_s}{100}, \quad (2)$$

$$e_s = 6.112 \times 10^{\left(\frac{7.5 \times T_d}{T_d + 237.3}\right)}, \quad (3)$$

where g is the acceleration due to gravity, q represents specific humidity (g/kg), and P_{i+1} and P_i are the pressures of the upper and lower layers (hPa), respectively. e_s is the saturated vapor pressure (hPa), RH is the relative humidity, and T_d is the atmospheric temperature in Celsius ($T_d = T + 273.15$).

2.2. GNSS PWV

The GNSS observations are collected from CMONOC using the GAMIT high-precision data processing software (ver 10.71). The zenith tropospheric delay (ZTD) [33] consists of the zenith hydrostatic delay (ZHD) and zenith wet delay (ZWD), and the ZHD can be obtained from the following formula [34]:

$$ZTD = ZHD + ZWD, \quad (4)$$

$$ZHD = \frac{2.2767 \times P_s}{1 - 0.00266 \cos \varphi - 0.00028 \times h_0}, \quad (5)$$

where φ is the latitude of the GNSS site (radians), h_0 is the height of the GNSS site above sea level (km), and P_s is the surface pressure (hPa) interpolated from the nearest meteorological site (MET) to the GNSS site.

The basic formula for inverting PWV from GNSS observations is as follows [35]:

$$\text{PWV} = \Pi \cdot \text{ZWD}, \quad (6)$$

$$\Pi = \frac{10^6}{\rho_W R_v \left[\frac{k_3}{T_m} + k_2' \right]}, \quad (7)$$

where ρ_W is the density of liquid water of $1 \times 10^3 \text{ kg/m}^3$, R_v is the water vapor gas constant of $461.495 \text{ J} \cdot \text{kg}^{-1} \cdot \text{K}^{-1}$, and k_2' and k_3 are the empirical values of atmospheric physical parameters of $22.13 \pm 2.20 \text{ K/hPa}$ and $(3.739 \pm 0.012) \times 10^5 \text{ K}^2/\text{hPa}$, respectively.

T_m is the atmospheric weighted mean temperature [36–38] calculated from surface temperature (K) T_s , site elevation h , latitude φ (radian), days of the year DOY, and model coefficients a_i ($i = 1, 2 \dots 7$). And the specific T_m regional model in this study refers to Huang et al. [39].

$$T_m(T_s, h, \varphi, \text{DOY}) = a_0 + a_1 T_s + a_2 h + a_3 \varphi + a_4 \cos\left(\frac{2\pi \cdot \text{DOY}}{365.25}\right) + a_5 \sin\left(\frac{2\pi \cdot \text{DOY}}{365.25}\right) + a_6 \cos\left(\frac{4\pi \cdot \text{DOY}}{365.25}\right) + a_7 \sin\left(\frac{4\pi \cdot \text{DOY}}{365.25}\right), \quad (8)$$

Given the limited number of GNSS sites equipped with meteorological instruments and the spatiotemporal resolution constraints of the RS dataset, the dataset from MET sites was utilized to derive T_m values for GNSS PWV inversion. The aforementioned meteorological parameters are provided by the China Meteorological Administration (CMA). The GNSS and MET sites are not collocated; hence, we utilize observations from the nearest MET sites to compute corresponding values at GNSS sites for GNSS PWV inversion [40].

$$T_s = T_0 - \beta(h - h_0), \quad (9)$$

$$P_s = P_0 \left[1 - \frac{\beta}{T_0} (h - h_0) \right]^{\frac{g \cdot M}{R \cdot \beta}}, \quad (10)$$

$$g = 9.8063 \cdot \left\{ 1 - 10^{-7} \frac{h + h_0}{2} \left[1 - 0.0026373 \cdot \cos(2\varphi) + 5.9 \cdot 10^{-6} \cdot \cos^2(2\varphi) \right] \right\}, \quad (11)$$

$$\beta(\varphi, \theta, \text{DOY}) = \delta_1 + \delta_2 \varphi + \delta_3 \theta + \delta_4 \cos\left(2\pi \frac{\text{DOY}}{365.25}\right) + \delta_5 \sin\left(2\pi \frac{\text{DOY}}{365.25}\right) + \delta_6 \cos\left(4\pi \frac{\text{DOY}}{365.25}\right) + \delta_7 \sin\left(4\pi \frac{\text{DOY}}{365.25}\right), \quad (12)$$

where T_s and T_0 are the temperature (K) at the GNSS site and MET site, P_s and P_0 are the pressure (hPa) at the GNSS site and MET site, and h and h_0 are the elevation (m) at the GNSS site and MET site, respectively. M is the molar mass of dry air, which is $0.02896444 \text{ kg/m}^3$, and R is the ideal gas constant, which is $8.31432 \text{ J/K} \cdot \text{mol}$. g is the gravitational coefficient and β is the lapse rate parameter. φ , θ , and DOY are the latitude, longitude (radian), and days of the year, respectively. δ_1 , δ_2 , δ_3 , δ_4 , δ_5 , δ_6 and δ_7 are the model coefficients.

The elevation difference, arising from the use of the geopotential height system for RS observations and the geodetic height system for GNSS observations, is a critical factor influencing the comparison results of different PWV datasets. The method proposed by Wang et al. [41] was adopted to standardize the height of the PWV dataset to the geodetic height. We combined GNSS sites with nearest MET observations and screened site groups where the time series matched by over 80%, ensuring the inverted PWV has high spatiotemporal resolution and accuracy. Therefore, the PWV data from 245 GNSS sites

in China and surrounding regions were finally selected, ensuring coverage across diverse geographic regions with varying climatic conditions. The distribution of RS sites and GNSS sites in the research area is shown in Figure 1.

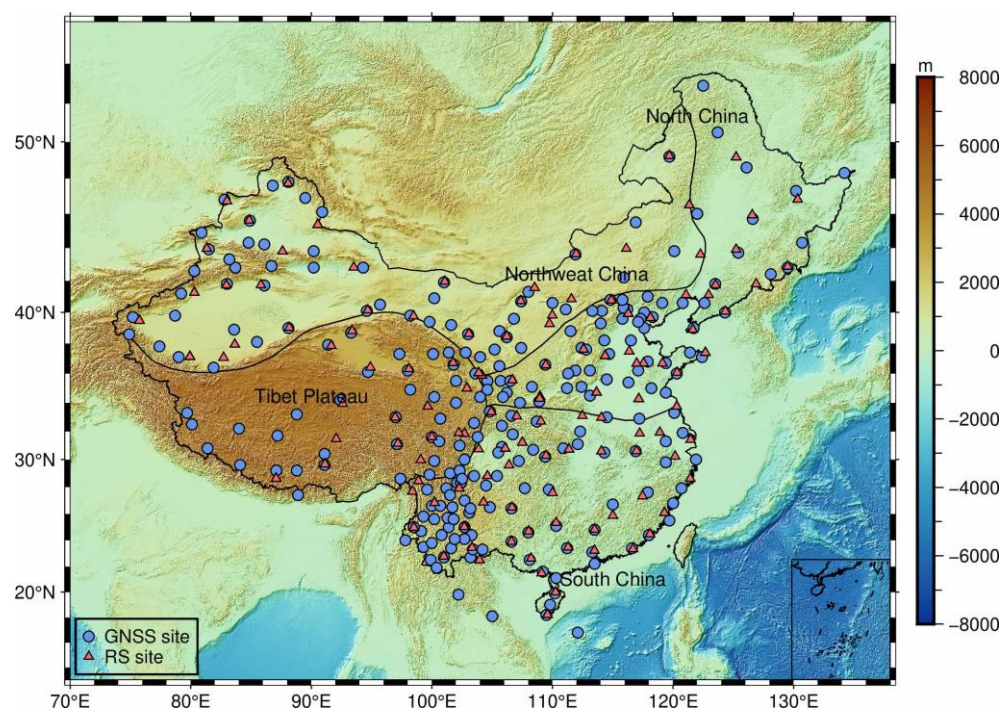


Figure 1. Distribution of RS sites and GNSS sites from 2019–2022 in the research area.

2.3. FY-4A PWV

The AGRI on the FY-4A can provide PWV retrieved from clear-sky atmospheric humidity profiles based on single pixels or $M \times M$ regions, and additional water vapor absorption channels enable it to monitor a richer range of water vapor content [26]. The spatial resolutions of the FY-4A PWV are 4 km, and the three flexible scanning modes of AGRI are shown in Figure 2: full disk (15 min), regional scan ($3\text{--}55^\circ\text{ N}$, $70\text{--}140^\circ\text{ E}$, 5 min), and static scan ($1000\text{ km} \times 1000\text{ km}$, 1 min). This study uses full disk FY-4A PWV data from 2019–2022, and the PWV product is available free of charge in near real-time from the official website. The most significant deviations in the FY-4A PWV data are primarily due to the challenges of satellite-based observations in accurately capturing atmospheric water vapor in regions with complex topography or dense cloud cover [42]. The preliminary data quality control of FY-4A PWV was conducted in accordance with official standards, with cloud regions (value: 65,534.0) and space view (value: 65,535.0) excluded.

The row-column matrix coordinates (x, y) of the FY-4A PWV product are converted to sub-satellite point latitude and longitude coordinates (Lat, Lon), then PWV gridded data closest to each site were extracted. To reduce the impact of random errors in FY-4A PWV, the average of the 3×3 gridded data centered around the nearest site grid point is used as the PWV value at the central grid point for PWV assessment [43,44].

$$\eta = \frac{\pi \times (\text{col} - \text{COFF})}{180 \times 2^{-16} \times \text{CFAC}'} \quad (13)$$

$$\zeta = \frac{\pi \times (\text{line} - \text{LOFF})}{180 \times 2^{-16} \times \text{LFAC}'} \quad (14)$$

where η and ζ are the scaling factors, col is the nominal row number, and line is the nominal column number. COFF is the column offset, CFAC is the column scaling factor, LOFF is the

row offset, and LFAC is the row scaling factor. The spatial resolution of the FY-4A PWV is 4 km; hence, the values of COFF, CFAC, LOFF, and LFAC are 1373.5, 10,233,137, 1373.5, and 10,233,137, respectively.

$$\begin{cases} S_d = \sqrt{(h \times \cos(\eta) \times \cos(\zeta))^2 - \left(\cos^2(\zeta) + \frac{ea^2}{eb^2} \times \sin^2(\zeta)\right) \times (h^2 - ea^2)} \\ S_n = \frac{h \times \cos(\eta) \times \cos(\zeta) - S_d}{\cos^2(\zeta) + \frac{ea^2}{eb^2} \times \sin^2(\zeta)} \\ S_1 = h - S_n \times \cos(\eta) \times \cos(\zeta) \\ S_2 = S_n \times \sin(\eta) \times \cos(\zeta) \\ S_3 = -S_n \times \sin(\zeta) \\ S_{xy} = \sqrt{S_1^2 + S_2^2} \end{cases}, \quad (15)$$

where h is the distance from the Earth’s center to the satellite center of mass, ea is Earth’s equatorial radius, $ea = 6378.137$ km and eb is Earth’s polar radius, $eb = 6356.7523$ km.

$$Lon = \frac{180}{\pi} \times \arctan\left(\frac{S_2}{S_1}\right) + \lambda_D, \quad (16)$$

$$Lat = \frac{180}{\pi} \times \arctan\left(\frac{ea^2}{eb^2} \times \frac{S_3}{S_{xy}}\right), \quad (17)$$

where Lon , Lat , and λ_D are the longitude, latitude, and longitude of the satellite subpoint, respectively.

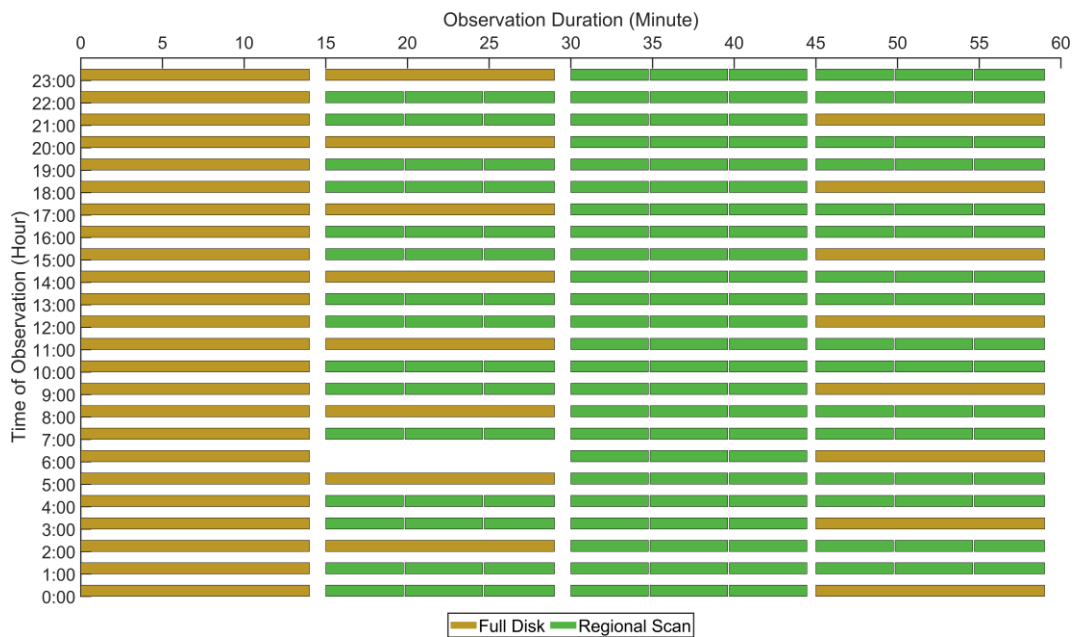


Figure 2. Observation mode of the AGRI on FY-4A satellite. The vertical axis represents UTC time in hours, while the horizontal axis represents the minutes within each hour.

2.4. Statistical Indicators

To analyze the discrepancies among various PWV datasets, the correlation coefficient (R), bias, RMSE, and MAE are calculated. Additionally, the PWV differences with their biases from the mean value larger than three times the standard deviation (STD) are removed as gross errors.

$$R = \frac{\sum_{i=1}^N (X_{O_i} - \bar{X}_O) (X_{R_i} - \bar{X}_R)}{\sqrt{\sum_{i=1}^N (X_{O_i} - \bar{X}_O)^2 \sum_{i=1}^N (X_{R_i} - \bar{X}_R)^2}}, \quad (18)$$

$$\text{Bias} = \frac{1}{N} \sum_{i=1}^N (X_{O_i} - X_{R_i}), \quad (19)$$

$$\text{RMSE} = \sqrt{\frac{1}{N} \sum_{i=1}^N (X_{O_i} - X_{R_i})^2}, \quad (20)$$

$$\text{MAE} = \frac{1}{N} \sum_{i=1}^N |X_{O_i} - X_{R_i}|, \quad (21)$$

where X_O represents the evaluated value, and X_R is the reference value.

3. Results and Discussion

After spatially and temporally matching FY-4A PWV with RS PWV and GNSS PWV, the RS PWV is initially considered as the reference value to assess the accuracy of FY-4A PWV products. Additionally, current research has confirmed that GNSS PWV and RS PWV exhibit comparable accuracy [45–47], with mean bias and RMSE values of 0.12 mm and 2.39 mm, respectively. Therefore, given the poorer spatiotemporal resolution of RS PWV, this study comprehensively evaluated FY-4A PWV using GNSS PWV as another reference.

3.1. Evaluation with RS PWV

Take RS PWV at UTC 0:00 and UTC 0:00 from 2019 to 2022 as the reference, the overall correlation (R), annual mean bias, and RMSE for FY-4A PWV in the CN, NC, NWC, SC, and TP regions are shown in Figure 3. The correlation between FY-4A PWV and RS PWV across the entire CN region is 0.80, with the annual mean bias ranging from 5.92 to 8.43 mm and the hourly mean bias varying from -7.71 to 12.43 mm each year. The annual mean biases for each year between FY-4A PWV and RS PWV are consistently positive, indicating that FY-4A PWV tends to overestimate water vapor values compared to RS PWV. The correlations between FY-4A PWV and RS PWV in the NC, NWC, SC, and TP subregions are 0.52, 0.72, 0.78, and 0.83, respectively. The annual mean biases of FY-4A PWV in the four subregions each year range from 5.21 to 7.73 mm, 5.79 to 7.04 mm, 6.41 to 10.02 mm, and 5.80 to 11.28 mm, with fluctuations of 2.41 mm, 1.25 mm, 3.61 mm, and 5.48 mm, respectively. The FY-4A PWV bias fluctuates significantly in the NC and NWC subregions with lower water vapor distribution, primarily due to the impact of sporadic extreme weather and abnormal rainfall on data accuracy [48].

For RMSE, FY-4A PWV in the CN region exhibits annual mean RMSE ranging from 7.88 to 9.64 mm and hourly mean RMSE ranging from 7.14×10^{-5} to 9.64 mm each year. The annual mean RMSE of FY-4A PWV each year in the NC, NWC, SC, and TP subregions ranges from 7.29 to 9.13 mm, 7.60 to 8.40 mm, 8.65 to 10.71 mm, and 7.36 to 11.36 mm, respectively, with fluctuations of 1.84 mm, 0.80 mm, 2.06 mm, and 4.00 mm. The minimum and maximum annual mean RMSE of FY-4A PWV are observed in the NC and TP subregions, respectively, with the lowest annual mean RMSE occurring in the TP subregion in 2019.

In Figure 3, the overall annual mean bias between FY-4A PWV and RS PWV in the CN, NC, NWC, SC, and TP regions were 7.21 mm, 6.25 mm, 6.29 mm, 7.98 mm, and 7.94 mm, with corresponding annual mean RMSE values of 7.03 mm, 7.07 mm, 6.93 mm, 7.05 mm, and 6.16 mm, respectively. FY-4A PWV significantly overestimates the actual PWV values

in the SC and TP regions, indicating that its detection capabilities remain inadequate in geographically complex areas, particularly in the rain-abundant southern regions and the climatically variable Tibetan Plateau, thus impacting the evaluation accuracy between different PWV datasets.

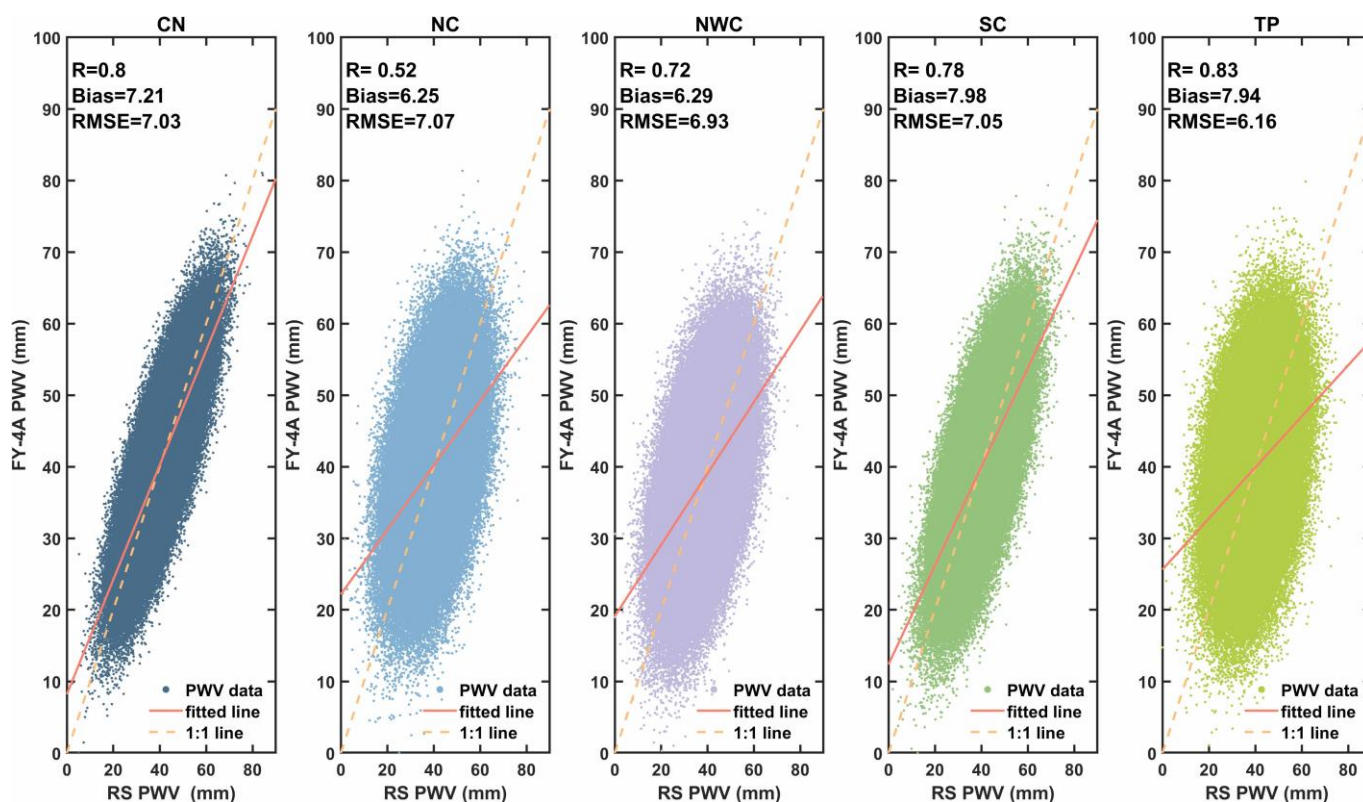


Figure 3. Fitting plots between RS PWV and FY-4A PWV from 2019 to 2022 for different regions, with correlation, annual mean bias, and RMSE values.

The intended trajectory of radiosonde balloons can be disrupted by mountainous terrain, affecting measurement accuracy, and artificial surfaces and buildings in urban areas can interfere with signal reception by remote sensing satellites. To investigate the accuracy performance of FY-4A PWV across different spatial scales, the distributions of annual mean bias and annual mean RMSE at various regional sites are presented in Figure 4 and summarized in Table 1. The annual mean bias and RMSE between FY-4A PWV and RS PWV at sites in the CN, NC, NWC, SC, and TP regions are 3.28 mm/7.31 mm, -0.08 mm/6.17 mm, 6.42 mm/6.83 mm, 2.46 mm/8.77 mm, and 7.31 mm/8.77 mm, respectively. The NC and NWC subregions exhibit smaller bias and RMSE values compared to the SC and TP subregions, with the FY-4A PWV bias in the NC subregion being negative, indicating higher overall accuracy in the NC and NWC subregions and an underestimation of water vapor values in the NC subregion. The high humidity and frequent rainfall in the SC subregion, coupled with the extreme climatic conditions and high altitude of the TP subregion, both contribute to significant challenges in achieving accurate water vapor detection across the entire study area.

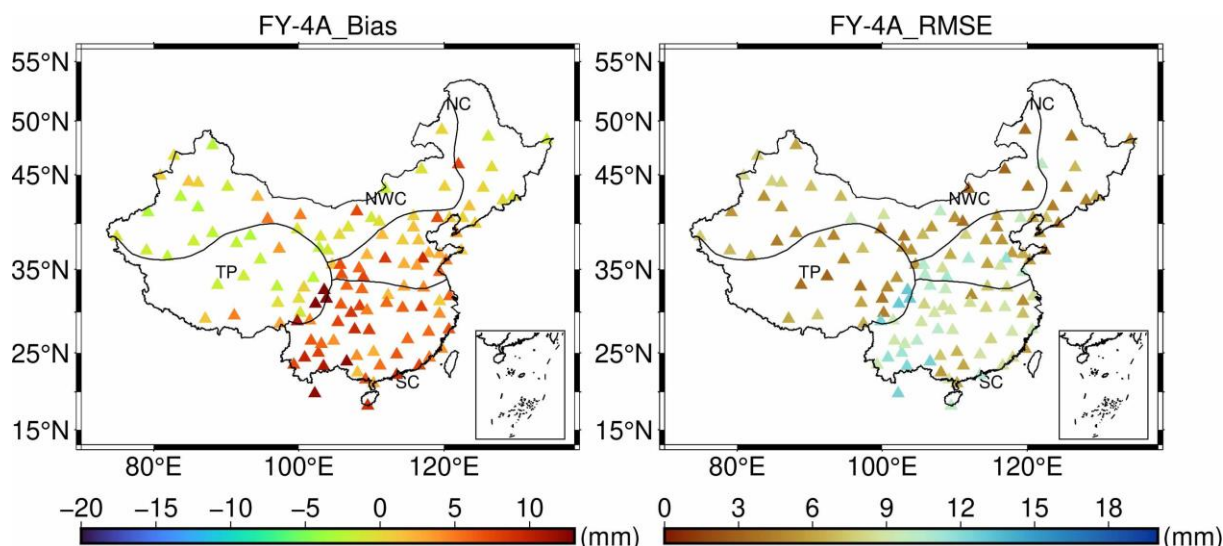


Figure 4. Site distribution maps of the mean bias and mean RMSE between FY-4A PWV and RS PWV from 2019 to 2022.

Table 1. Annual mean bias and annual mean RMSE of FY-4A PWV at sites across different regions compared to RS PWV.

Regions	Bias (mm)			RMSE (mm)		
	Min	Max	Mean	Min	Max	Mean
CN	−2.92	12.79	3.28	2.93	12.95	7.31
NC	−2.92	7.39	−0.08	3.34	10.04	6.17
NWC	−1.79	9.29	2.84	3.18	11.51	6.83
SC	0.91	12.36	6.42	4.91	12.47	8.77
TP	−2.91	12.79	2.46	2.93	12.95	6.82

In Figure 4, the NC subregion has the highest proportion of negative bias among the four subregions, while the SC region has the highest proportion of positive bias and no negative bias. The NC subregion exhibits the highest proportion of negative bias among the four subregions, whereas the SC region has the highest proportion of positive bias and no negative bias. The FY-4A PWV exhibits significant bias values at the TP subregion sites ‘56,172’, ‘56,187’, and ‘56,444’ with biases of 12.79 mm, 12.62 mm and 11.08 mm, and at the SC subregion sites ‘56,964’, ‘57,816’, and ‘59,211’, which are below 180 mm in altitude and situated dense urban building clusters, with biases of 9.80 mm, 9.49 mm and 12.36 mm, respectively. The urban heat island effect can lead to discrepancies between RS site measurements and those in suburban areas, while satellite remote sensing, due to its limited spatial resolution, may not capture localized microclimate effects, thus impacting the accuracy of PWV assessments. FY-4A PWV shows relatively high RMSE values widely distributed in the SC and TP subregions, with the highest RMSE of 12.47 mm at site ‘59,211’ in the SC subregion and the highest RMSE of 12.95 mm at site ‘56,173’ in the TP subregion.

To assess the contribution rates of various accuracy metrics for FY-4A PWV, histograms and statistical summaries of bias and RMSE across different regions are presented in Figure 5. Using RS PWV as the reference value, the mode of the bias and RMSE for FY-4A PWV in the CN region and their associated probability densities are −0.6 mm (16.80%) and 5.9 mm (17.6%). For the NC subregions, the mode of the bias and RMSE and their probability densities in the CN region are −2.5 mm/−0.2 mm (both 24.14%) and 5.5 mm/6.9 mm (both 17.24%), whereas, for the NWC subregions, the metrics are 2.2 mm (22.22%) and 5.9 mm (22.22%). Considering the accuracy distribution at the sites shown

in Figure 4, FY-4A PWV exhibits relatively stable accuracy across the entire study area in both the NC and NWC subregions, with the NC subregion showing a significantly more negative bias mode and a larger RMSE mode compared to the NWC subregion. For the SC subregions, the corresponding aforementioned accuracy metrics are 5.8 mm (21.95%) and 9.1 mm (29.27%), whereas for the TP subregions, they are -2.2 mm (31.58%) and 4.8 mm/12.4 mm (both 21.05%). This suggests that areas with high moisture levels and active water vapor movement tend to exhibit unstable water vapor detection accuracy.

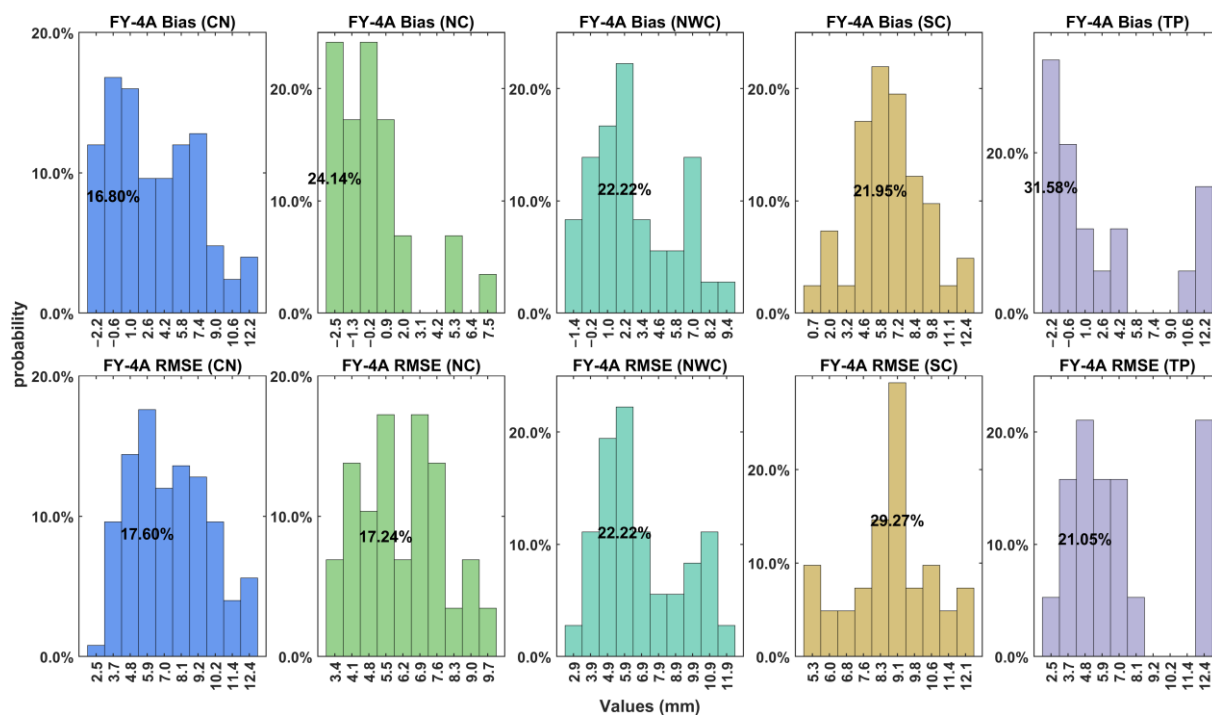


Figure 5. Histograms of annual mean bias and RMSE between FY-4A PWV and RS PWV in different regions.

3.2. Evaluation and Adjustment with GNSS PWV

3.2.1. Annual and Spatial PWV Variability

Given that RS sites only provide PWV data at UTC 0:00 and UTC 12:00, limiting the assessment of FY-4A PWV accuracy at higher temporal resolutions, this section will use GNSS PWV as the reference to evaluate the accuracy of FY-4A PWV over short to medium time scales. We employed seasonal average PWV data from FY-4A satellites and GNSS sites for 2022, as depicted in Figure 6, to effectively illustrate the spatial characteristics of water vapor distribution across diverse geographical regions. As shown in Figure 6, the overall distribution trends of FY-4A PWV and GNSS PWV across different seasons are consistent. However, the relatively sparse distribution of GNSS stations in some remote and coastal areas may explain the significant discrepancies between the two datasets. The differences in the measurement systems (e.g., GNSS versus satellite-based sensors) may, additionally, account for some of these deviations, as they rely on distinct retrieval methods and make varying assumptions about the atmospheric profile. The fitted correlation (R), mean bias, and mean RMSE between FY-4A PWV and GNSS PWV with an hourly temporal resolution (UTC 0:00 to UTC 23:00) from 2019 to 2022 across different regions are presented in Figure 7.

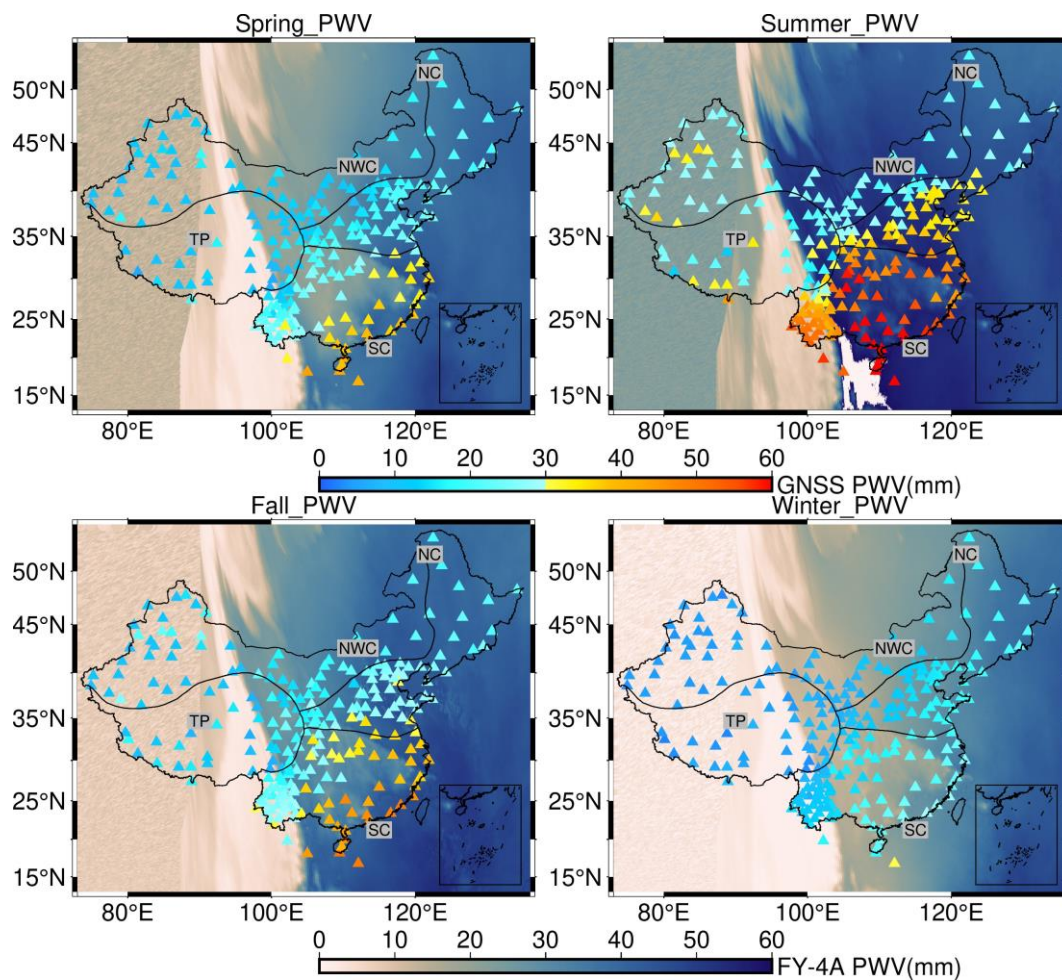


Figure 6. Seasonal average distribution of FY-4A PWV and GNSS PWV for 2022.

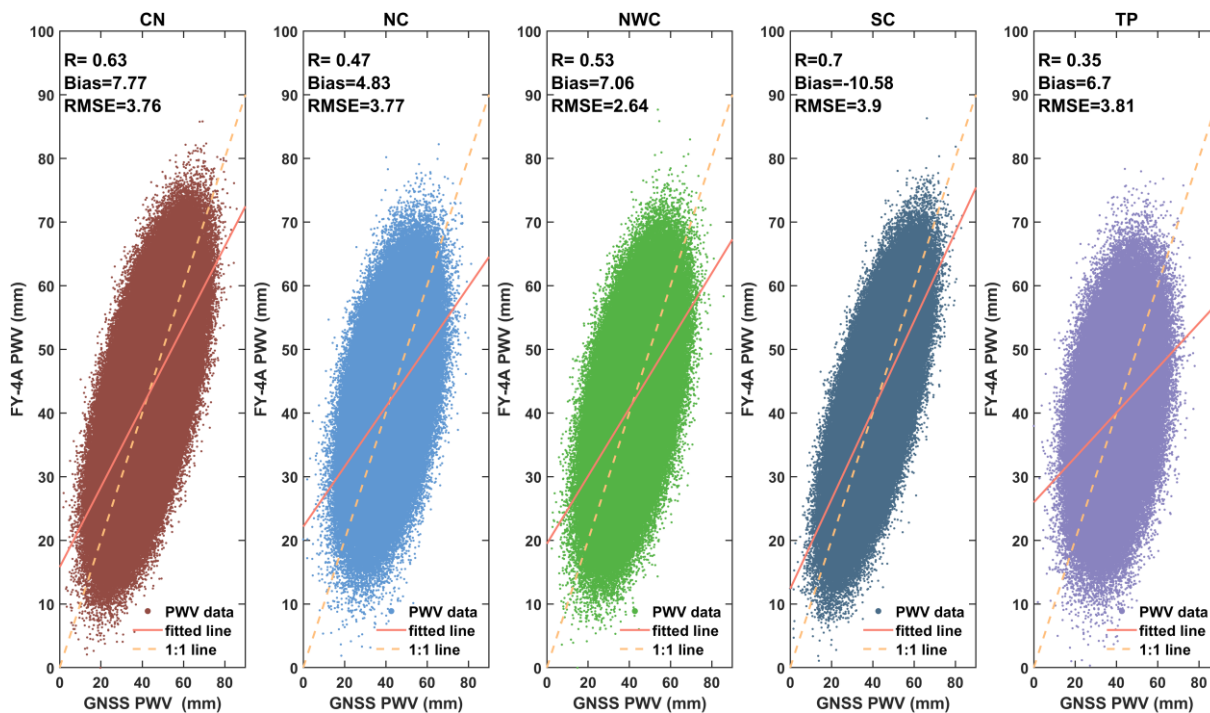


Figure 7. Fitting plots between FY-4A PWV and GNSS PWV from 2019 to 2022 for different regions, with correlation, annual mean bias, and RMSE values.

Taking GNSS PWV as the reference value, the annual mean bias and RMSE of FY-4A PWV at 245 sites are listed in Table 2, and the spatial distribution is shown in Figure 8. In Table 2, the ranges of the annual mean bias and RMSE between FY-4A PWV and GNSS PWV at sites in the CN region, as well as the corresponding averages, are from -5.80 mm to 10.14 mm (1.39 mm) and from 4.23 mm to 15.28 mm (8.22 mm), respectively. Additionally, the mean bias and RMSE in NC, NWC, SC, and TP subregions are 2.36 mm/ 3.85 mm/ -1.51 mm/ 2.12 mm, and 7.97 mm/ 9.52 mm/ 7.79 mm/ 7.37 mm, respectively. In Figure 8, the proportions of sites with negative annual mean bias in the CN, NC, NWC, SC, and TP regions are 37%, 18%, 6%, 79%, and 28%, respectively, indicating that most sites in the SC subregions tend to underestimate the annual water vapor values. Moreover, large absolute negative bias values are predominantly found along the coastline and in the Guangxi and Yunnan regions of China, while substantial positive bias values are primarily observed at sites ‘QHGE’ and ‘XZGE’ in the TP subregion, as well as at sites ‘CHUN’, ‘XLHG’ and ‘NMER’ in the NWC subregion. For RMSE, smaller values are predominantly distributed at the TP region sites ‘QHYS’, ‘SCGZ’, and ‘QHDL’, while larger values are mostly found at the NC region sites ‘HECC’ and ‘BJYQ’.

Table 2. Annual mean bias and annual mean RMSE of FY-4A PWV at sites across different regions compared to GNSS PWV.

Regions	Bias (mm)			RMSE (mm)		
	Min	Max	Mean	Min	Max	Mean
CN	-5.80	10.14	1.39	4.23	15.28	8.22
NC	-2.38	10.14	2.36	4.81	15.28	7.97
NWC	-3.86	8.35	3.85	6.01	12.80	9.52
SC	-5.80	4.92	-1.51	5.06	11.05	7.79
TP	-3.90	8.49	2.12	4.23	11.12	7.37

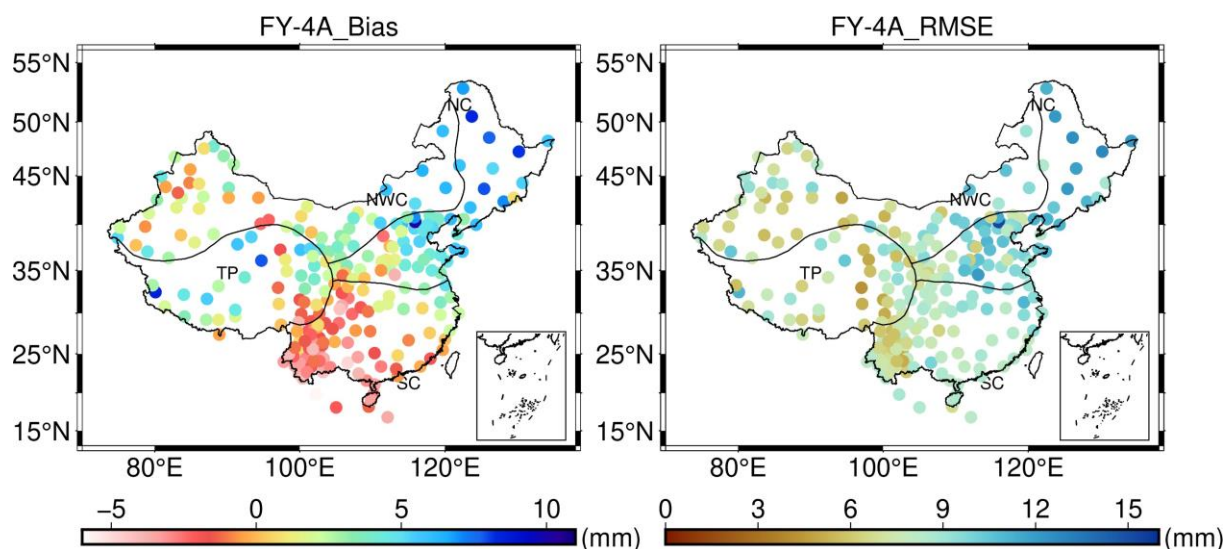


Figure 8. Site distribution maps of the mean bias and mean RMSE between FY-4A PWV and GNSS PWV from 2019 to 2022.

The discrepancies are driven by factors such as signal attenuation from cloud layers [49], the scattering effects of precipitation, and variations in satellite sensor sensitivity under different atmospheric conditions. As shown in Figure 7, the correlation in the TP subregion is the lowest, further suggesting that extreme climatic conditions and terrain interference in this area may adversely affect the performance of satellite sensor infrared channels and the accuracy of water vapor detection. The range of overall annual mean bias

and RMSE between FY-4A PWV and GNSS PWV across different regions, along with their corresponding variability, is from -11.19 mm to -4 mm (with a fluctuation of 5.57 mm) and from 2.67 mm to 3.98 mm (1.26 mm), respectively. Although the correlation between FY-4A PWV and GNSS PWV is lower in the TP subregion compared with the SC subregion, the highest mean bias and mean RMSE are found in the SC subregion. This indicates that seasonal water vapor variability is more pronounced in the SC subregion, which is more influenced by monsoons compared to the TP subregion, and the higher water vapor content in the SC subregion results in a greater range of PWV variations, posing a challenge to the sensitivity of water vapor detection equipment.

3.2.2. Seasonal and Spatial PWV Variability

To investigate the monthly-scale accuracy and seasonal variation characteristics of FY-4A PWV, the monthly mean bias and RMSE between FY-4A PWV and GNSS PWV are illustrated in Figure 9 and summarized in Table 3. Taking GNSS PWV as the reference value, the monthly mean bias range of FY-4A PWV across the entire study area is -11.9 to 12.2 mm, -12.37 to 24.96 mm, -12.72 to 17.8 mm, and -13.09 to 10.26 mm for the four seasons, with a corresponding mean bias of 2.82 mm, 7.22 mm, 5.55 mm, and 1.73 mm, respectively. FY-4A PWV exhibits a positive mean bias in all four seasons, indicating that it is generally higher than GNSS PWV throughout the year, with the absolute value of the mean bias being largest in summer, reaching 8.42 mm in July and 8.74 mm in August.

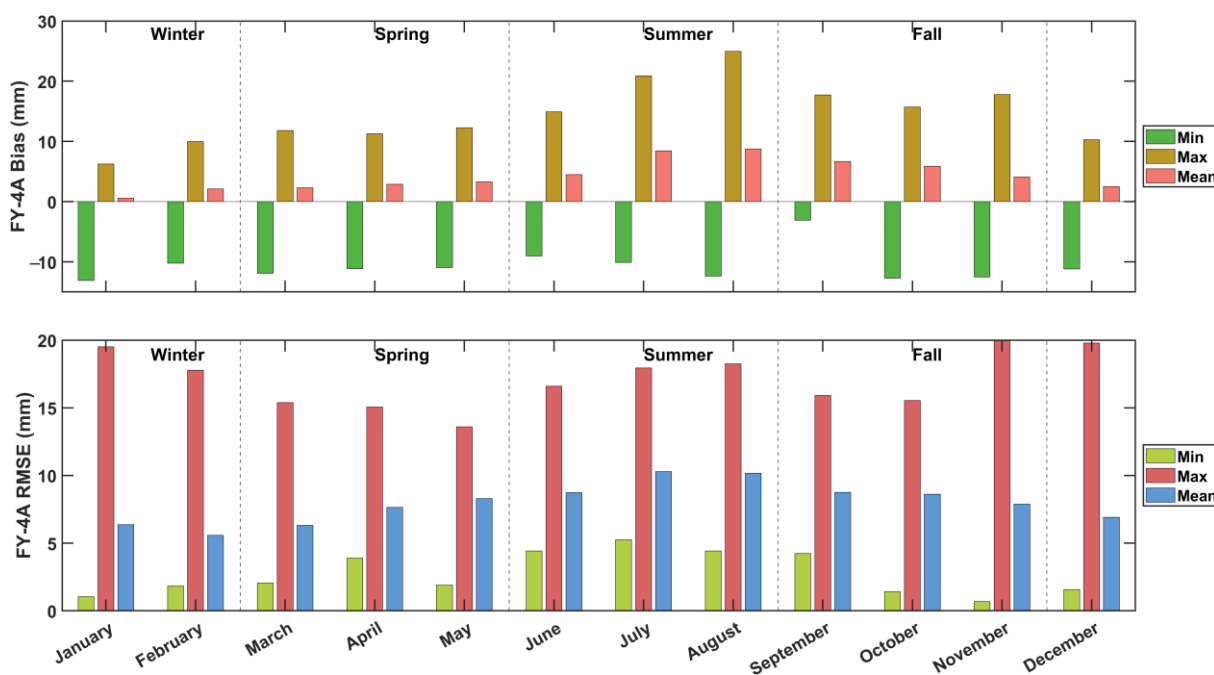


Figure 9. Bar charts of monthly mean bias and RMSE for four seasons between FY-4A PWV and GNSS PWV from 2019–2022.

In Figure 9 and Table 3, the monthly mean RMSE between FY-4A PWV and GNSS PWV for four different seasons are 7.42 mm, 9.73 mm, 8.42 mm, and 6.29 mm, respectively. Analysis of the monthly mean RMSE trends reveals that the RMSE for FY-4A PWV rose from 6.32 mm in March to 8.3 mm in May, indicating a gradual increase in error throughout the spring. In summer, the RMSE peaked at 8.74 mm in June and further increased to 10.29 mm in July before slightly decreasing to 10.17 mm in August, reflecting higher and more variable RMSE. It then decreased from 8.75 mm in September to 7.89 mm in November, suggesting improved accuracy with the arrival of autumn. During winter, the

RMSE continued to decline, dropping from 6.92 mm in December to 5.59 mm in February, indicating that FY-4A PWV achieves relatively higher accuracy in the winter months.

Table 3. Statistics of monthly mean bias and RMSE between FY-4A PWV and GNSS PWV in Spring, Summer, Fall, and Winter from 2019 to 2022.

Season\Month		Bias (mm)			RMSE (mm)		
		Min	Max	Mean	Min	Max	Mean
Spring	3	−11.90	11.82	2.29	2.05	15.38	6.32
	4	−11.15	11.26	2.87	3.89	15.07	7.64
	5	−10.97	12.28	3.30	1.90	13.60	8.30
Summer	6	−9.03	14.91	4.50	4.43	16.59	8.74
	7	−10.13	20.90	8.42	5.26	17.95	10.29
	8	−12.37	24.96	8.74	4.43	18.26	10.17
Autumn	9	−3.08	17.73	6.66	4.23	15.92	8.75
	10	−12.72	15.73	5.88	1.43	15.54	8.62
	11	−12.51	17.80	4.11	0.69	20.72	7.89
Winter	12	−11.17	10.26	2.50	1.57	19.78	6.92
	1	−13.09	6.26	0.59	1.05	19.52	6.37
	2	−10.24	9.96	2.10	1.84	17.78	5.59

To investigate the seasonal accuracy variability of FY-4A PWV across different regions, the monthly mean bias and RMSE between FY-4A PWV and GNSS PWV in each subregion are presented in Figure 10. As shown in Figure 10, the monthly mean bias and RMSE between FY-4A PWV and GNSS PWV in different subregions for spring, summer, autumn, and winter are as follows: in the NC subregion, the metrics are 6.25 mm/13.37 mm/5.30 mm/4.17 mm and 4.98 mm/8.16 mm/10.50 mm/6.03 mm, respectively; in the NWC subregion, they are 6.25 mm/13.37 mm/5.30 mm/4.17 mm and 8.58 mm/10.43 mm/8.50 mm/11.08 mm, respectively; in the SC subregion, they are 3.90 mm/11.40 mm/4.36 mm/5.00 mm and 5.83 mm/8.45 mm/8.26 mm/7.91 mm, respectively; in the TP subregion, they are 3.62 mm/5.27 mm/8.46 mm/1.69 mm and 3.98 mm/10.24 mm/7.69 mm/4.51 mm, respectively.

The monthly mean bias and RMSE of FY-4A PWV exhibit distinct seasonal and geographical characteristics, with longer boxes in July and August across most regions, indicating that the differences between FY-4A PWV and GNSS PWV are more dispersed and exhibit greater variability during the summer. Moreover, FY-4A PWV exhibits the highest absolute bias and RMSE during the summer across all subregions, except for the highest RMSE observed in the NC subregion during autumn and the NWC subregion during winter. This suggests that higher summer temperatures increase the atmosphere's capacity for water vapor, and frequent convective activities lead to intense localized precipitation, making it more challenging to capture seasonal water vapor variations. Moreover, residual summer convective activity, along with decreasing temperatures in autumn and winter and reduced vegetation cover, can affect the data quality of meteorological satellites in the NC and NWC subregions.

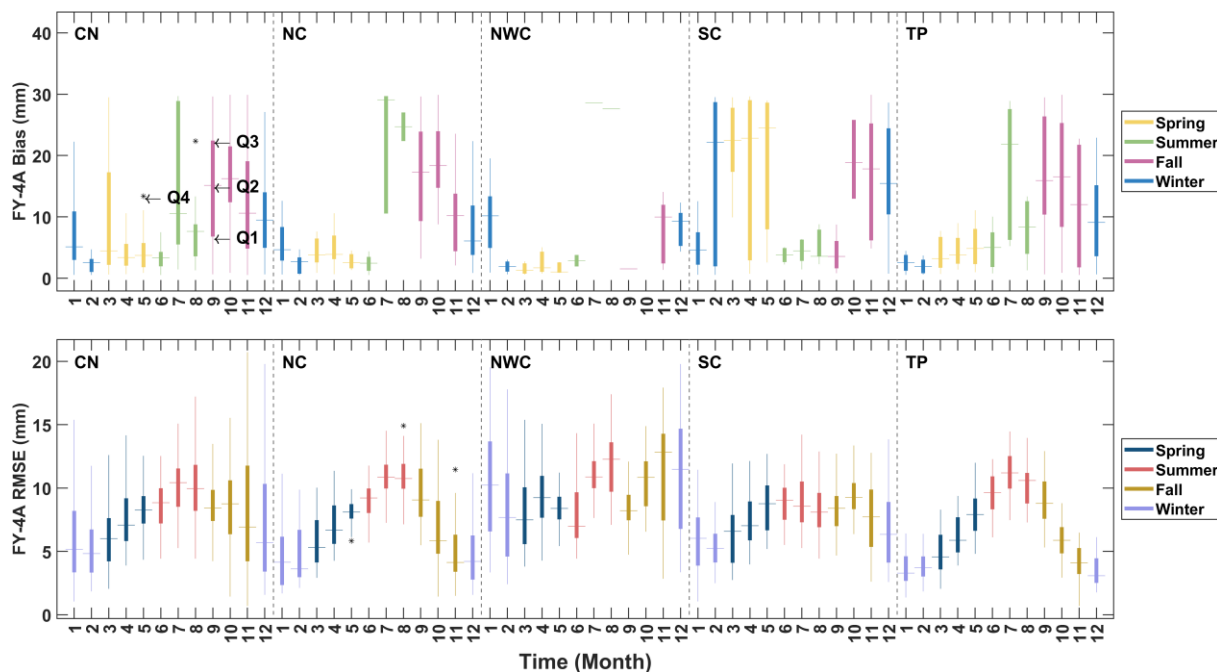


Figure 10. Box plots of monthly mean bias and RMSE between FY-4A PWV and GNSS PWV from 2019–2022 in different regions. Q1 and Q3 of the box are the first and third quartiles, respectively. The distance between Q1 and Q3 reflects the degree of fluctuation of the data; Q2 is the median value, which reflects the average level of the data; Q4 is the outlier.

3.2.3. Diurnal and Spatial PWV Variability

To evaluate the accuracy of FY-4A PWV at a finer temporal scale, using GNSS PWV as the reference, the daily bias and daily RMSE of FY-4A PWV across different regions are summarized in Table 4. In Table 4, the daily bias and RMSE between FY-4A PWV and GNSS PWV across the entire study area and the four subregions range from -4.45 mm to 9.47 mm and from 0 mm to 12.00 mm, respectively. Furthermore, the daily mean bias and RMSE of FY-4A PWV in the CN, NC, NWC, SC, and TP regions are 0.56 mm/ 0.52 mm/ 0.29 mm/ -0.57 mm/ 2.01 mm and 2.59 mm/ 2.17 mm/ 1.51 mm/ 3.19 mm/ 3.51 mm, respectively. FY-4A PWV exhibits a positive daily mean bias in the three subregions except for the SC subregion, suggesting significant regional differences in accuracy assessment and a tendency to overestimate water vapor content.

Table 4. Statistics of daily bias and daily RMSE between FY-4A PWV and GNSS PWV in different regions from 2019 to 2022.

Region	Bias (mm)			RMSE (mm)		
	Min	Max	Mean	Min	Max	Mean
CN	-4.03	9.47	0.56	0.00	12.00	2.59
NC	-1.84	3.84	0.52	0.44	7.30	2.17
NWC	-3.12	5.33	0.29	0.00	6.59	1.51
SC	-4.45	4.50	-0.57	0.63	7.91	3.19
TP	-3.95	5.33	2.01	0.36	12.00	3.51

Taking GNSS PWV from 2019 to 2022 as the reference, the time series of daily mean bias and daily mean RMSE of FY-4A PWV in different regions are shown in Figure 11. As shown in Figure 11, FY-4A PWV exhibits distinct seasonal variations in daily mean bias and RMSE across different regions, with smaller and more stable values in autumn and winter,

as well as notable spikes and irregular fluctuations during the summer. Additionally, the percentage of days with a negative daily mean bias for FY-4A PWV is 18%, 21%, 67%, and 31% of the annual time series in the NC, NWC, SC, and TP subregions, respectively. Combining the metrics from Table 4, the tendency of FY-4A PWV to underestimate water vapor on a daily scale shows notable regional differences, with more significant underestimation observed in the SC and TP subregions compared to the NC and NWC subregions.

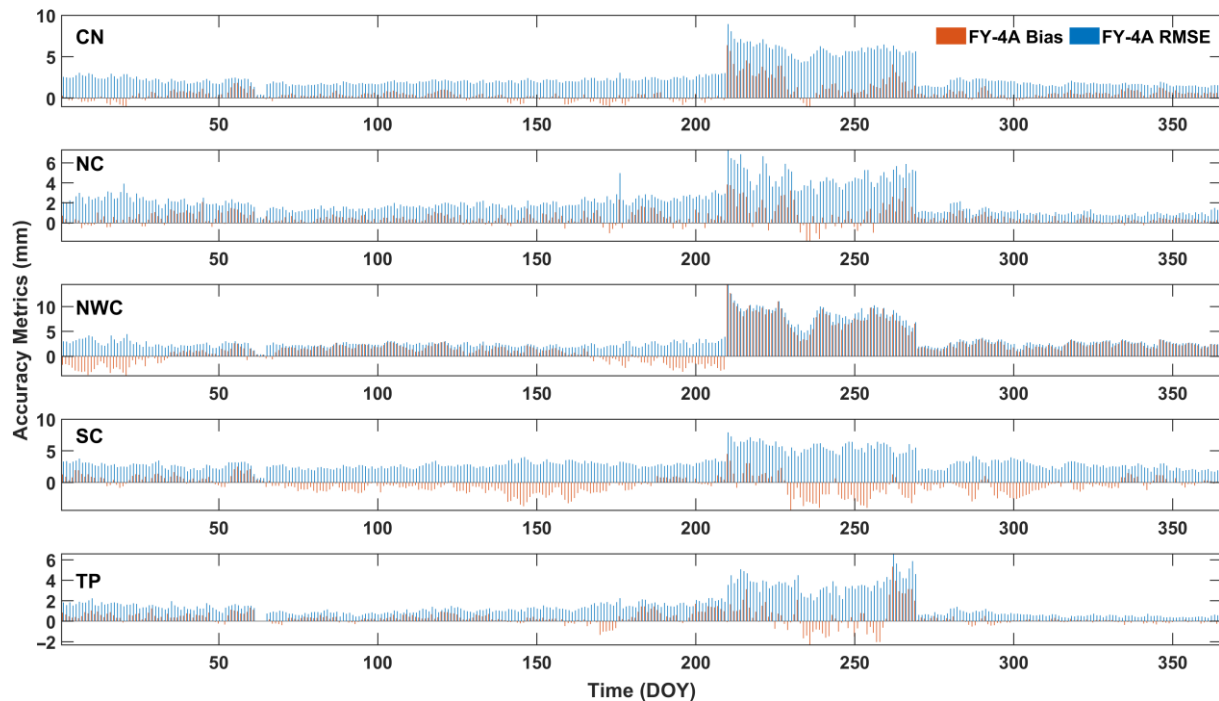


Figure 11. Time series of daily mean bias and RMSE between FY-4A PWV and GNSS PWV in different regions from 2019 to 2022.

3.2.4. FY-4A PWV Adjustment Model

The analysis of the evaluation results indicates that the biases between FY-4A PWV and GNSS PWV exhibit seasonal variations across different subregions. This study constructed an adjustment model for FY-4A PWV based on GNSS PWV using the linear correction method commonly employed in previous research [50,51]. The adjustment model was developed using the PWV dataset from 2019 to 2021, with the 2022 PWV dataset subsequently used to evaluate the model's accuracy performance.

$$PWV_{ADJ} = a \times PWV_{ORI} + b. \quad (22)$$

where PWV_{ORI} represents FY-4A PWV, PWV_{ADJ} is the corrected FY-4A PWV, and a and b are the model coefficients, with their specific values provided in Table 5.

Table 5. Statistics of model coefficients for the correction of FY-4A PWV using GNSS PWV across five subregions and four seasons. (a, b) represent the coefficients of the model Equation (21).

	Spring (a, b)		Summer (a, b)		Fall (a, b)		Winter (a, b)	
CN	0.56	9.71	0.63	12.37	0.67	9.54	0.53	7.50
NC	0.15	10.36	0.16	21.31	0.44	9.24	0.07	6.24
NWC	0.35	15.38	0.31	20.56	0.39	18.20	0.22	14.09
SC	0.62	8.68	0.65	15.74	0.75	7.50	0.53	8.08
TP	0.36	8.19	0.50	13.11	0.57	6.29	0.31	4.23

Figure 12 illustrates the correction performance of the commonly used linear adjustment model for FY-4A PWV, with GNSS PWV as the reference, by presenting the mean MAE, RMSE, and their improvement rates before and after correction. The MAE and RMSE between the corrected FY-4A PWV and GNSS PWV decreased to varying extents across all regions and seasons. The correction model, notably, demonstrated the most significant improvement during summer in the entire CN region compared to other seasons. The seasonal adjustment models for the NWC subregion show the most significant improvement among the four subregions throughout the year, with mean MAE and RMSE reduced by 4.05 mm (48.83%) and 4.93 mm (48.16%) in summer, respectively. The minimum mean bias between the corrected FY-4A PWV and GNSS PWV is 0.40 mm, -0.12 mm, 0.14 mm, 0.10 mm, and -0.08 mm in the CN, NC, NWC, SC, and TP regions, respectively, with the majority of these values occurring in winter. Additionally, the RMSE between the corrected FY-4A PWV and GNSS PWV in spring and winter for each subregion is approximately 6 mm, indicating that the corrected FY-4A PWV meets the requirements for meteorological applications [48,52], and the corresponding subregional adjustment model is practical.

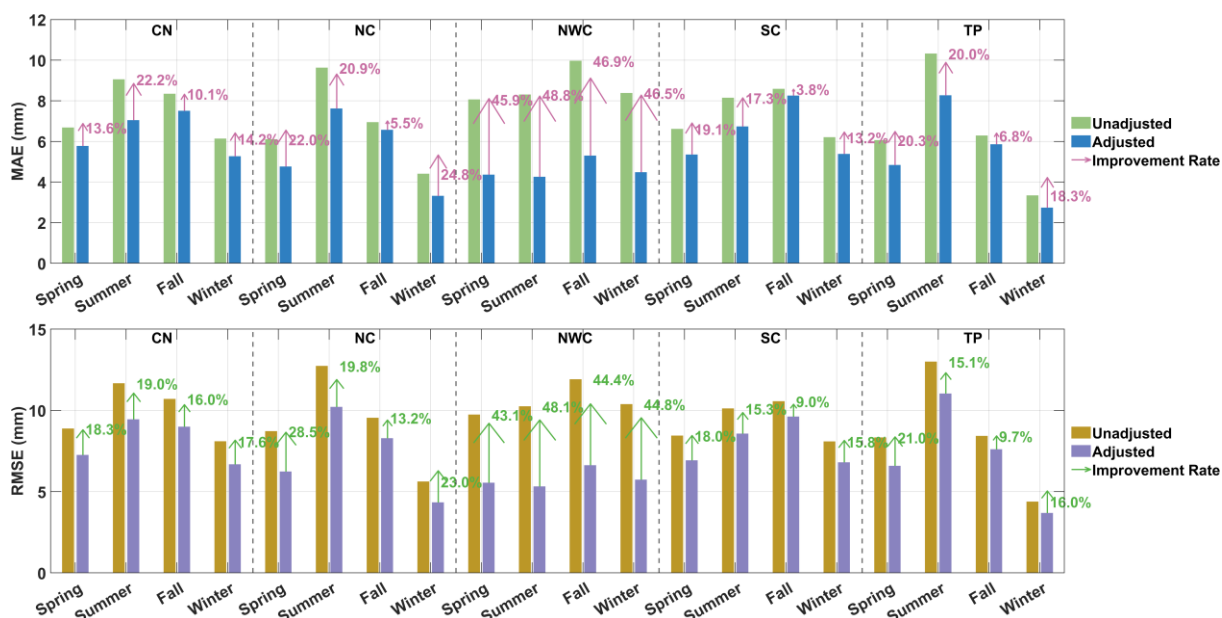


Figure 12. Bar charts of the mean MAE and RMSE between FY-4A PWV and GNSS PWV before and after adjustment in different regions and seasons for 2022. The length of the arrows represents the degree of improvement in mean MAE and RMSE.

Figure 13 shows the site-level distribution of improvements in MAE and RMSE for corrected FY-4A PWV, based on regional adjustment models for different seasons, using GNSS PWV as the reference and compared to the uncorrected data. The improved MAE across all regions reaches a maximum of 8.28 mm in spring, 12.77 mm in summer, 10.36 mm in autumn, and 10.21 mm in winter, while the corresponding improved RMSE maximum values are 8.28 mm, 12.90 mm, 10.02 mm, and 9.89 mm, respectively. The range of RMSE improvements in spring is the widest in the NWC region, as shown in the statistics in Table 6, while the range of MAE and RMSE improvements exhibits the widest distribution in summer for all other subregions. The performance of the regional adjustment model in summer shows a significant improvement at most sites across the subregions. The stations exhibiting the most significant seasonal improvements are: ‘HRBN’, ‘SDCY’, and ‘SDRC’ in the NC subregion; ‘GSGT’, ‘XJBL’, and ‘XJWQ’ in the NWC subregion; ‘JSYC’, ‘ZJWZ’, and ‘GDZJ’ in the SC subregion; and ‘QHME’, ‘QHMY’, and ‘XZZB’ in the TP subregion. The majority of these stations are situated along the eastern coastline of the study area, where

water vapor distribution is characterized by complex variations, and in the western regions at elevations exceeding 3000 m.

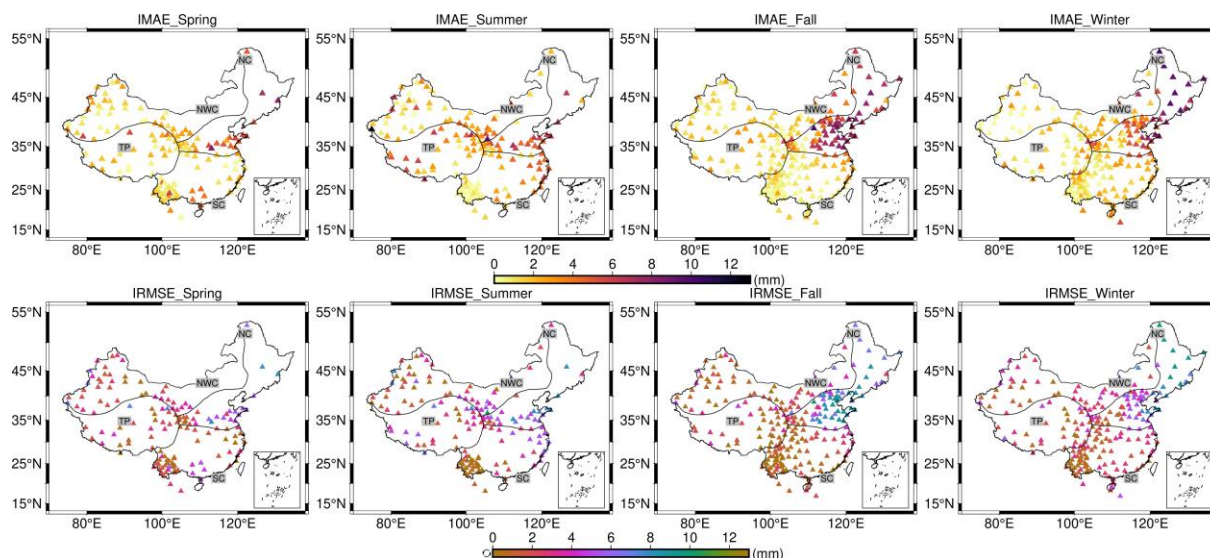


Figure 13. Site-level distribution of seasonal average improvements in MAE and RMSE between corrected and uncorrected FY-4A PWV and GNSS PWV for 2022. IMAE and IRMSE represent the improved MAE and RMSE values, respectively.

Table 6. Statistics of the first quartile (Q1), third quartile (Q3), and interquartile range (IQR) for site-level MAE and RMSE improvements across different seasons in the four subregions.

IMAE (mm)	NC			NWC			SC			TP		
	Q1	Q3	IQR	Q1	Q3	IQR	Q1	Q3	IQR	Q1	Q3	IQR
Spring	0.67	2.61	1.94	1.77	5.09	3.32	0.48	2.08	1.59	0.5	2.26	1.76
Summer	0.87	3.52	2.65	2.02	5.72	3.7	0.21	3.38	3.16	1.99	5.02	3.03
Fall	0.68	1.94	1.26	4.47	7.34	2.87	0.29	1.45	1.16	0.38	1.99	1.61
Winter	0.34	2.05	1.71	3.47	7.02	3.54	0.62	2.24	1.62	0.48	1.7	1.22
IRMSE (mm)	NC			NWC			SC			TP		
	Q1	Q3	IQR	Q1	Q3	IQR	Q1	Q3	IQR	Q1	Q3	IQR
Spring	1.75	3.39	1.64	1.72	5.73	4.01	0.58	2.5	1.93	0.67	3.18	2.51
Summer	0.88	4.14	3.26	2.95	6.68	3.73	0.29	3.41	3.11	1.71	4.94	3.23
Fall	0.73	2.5	1.77	4.72	8.39	3.67	0.44	1.7	1.26	0.33	2.32	1.98
Winter	1.44	3.35	1.91	3.92	7.36	3.44	0.88	2.56	1.68	0.9	3.13	2.22

4. Conclusions

The reasonable application of high-precision multi-source PWV products is essential for numerical weather prediction [53,54], monitoring of extreme weather, and InSAR atmospheric correction [55,56]. However, the accuracy performance and spatiotemporal resolution of FY-4A PWV are significantly different from those of ground-based PWV, and comprehensive evaluation and analysis of long-term FY-4A PWV products for the China region are currently limited. This study evaluates the accuracy performance of FY-4A PWV products using PWV retrieval data from 125 RS sites and 245 GNSS sites in China and surrounding areas from 2019 to 2022, incorporating various time scales (such as annual, monthly, and daily averages) and spatial scales.

In the overall performance analysis, FY-4A PWV products showed significant associations with the PWV values retrieved by RS and GNSS. Using RS PWV as a reference value, the overall annual mean bias and RMSE of FY-4A PWV across the entire study area are

7.21 mm and 7.03 mm, respectively. To investigate the impact of geographic and climatic factors on the accuracy assessment of FY-4A PWV products, the biases and RMSEs at RS sites for the NC, NWC, SC, and TP subregions are -0.08 mm/ 6.42 mm/ 2.46 mm/ 7.31 mm and 6.17 mm/ 6.83 mm/ 8.77 mm/ 8.77 mm, respectively. The NC and NWC subregions show lower bias and RMSE, whereas high humidity, frequent rainfall in the SC subregion, and extreme climate and altitude in the TP subregion pose significant challenges for accurate water vapor detection across the study area. Given that differences in the distribution density of RS sites across subregions can affect the representativeness and accuracy of water vapor data, these variations should be considered in the analysis and evaluation of the data.

Taking GNSS PWV as a reference value, the annual mean bias and RMSE of FY-4A PWV across the entire study area are -8.85 mm and 3.76 mm, respectively. Moreover, the assessment accuracy of FY-4A PWV exhibits obvious seasonal and regional distribution characteristics across the entire study area. At a monthly scale across the four seasons, the mean bias and RMSE are 2.82 mm/ 7.42 mm in spring, 7.22 mm/ 9.73 mm in summer, 5.55 mm/ 8.42 mm in autumn, and 1.73 mm/ 6.29 mm in winter. In addition, the daily mean bias and RMSE in summer exhibit noticeable peaks and irregular fluctuations compared to autumn and winter. For the accuracy metrics at GNSS sites across different subregions, FY-4A PWV at sites in the SC subregion generally underestimates annual water vapor compared to GNSS PWV, with many of these sites located in low-latitude regions and near the coastline.

In summary, FY-4A PWV products, with the advantages of high spatiotemporal resolution and moderate accuracy, can serve as a valuable complement to site-based PWV measurements and hold significant application potential. The commonly used linear adjustment model significantly improved the accuracy of FY-4A PWV based on GNSS PWV across the entire study area. Notably, the model showed the greatest improvement in the NWC subregion from a regional perspective and in summer from a seasonal perspective. Future research will aim to calibrate FY-4A PWV data, especially under cloudy and rainy conditions, integrate FY-4A PWV with ground-based PWV data, conduct reanalyses of gridded PWV data, as well as assess their application on short-term heavy rainfall forecasting.

Author Contributions: L.H., W.L. and X.C.: conceptualization, methodology, and formal analysis; C.L.: software; X.C. and Y.Y.: validation; C.T. and C.L.: investigation; C.T.: resources; W.L.: data curation; W.L. and X.C.: writing—original draft preparation; Y.Y. and W.L.: writing—review and editing; L.L., L.H. and S.X.: funding acquisition. All authors have read and agreed to the published version of the manuscript.

Funding: This study is supported by the Guangxi Science and Technology Program (Guike AA24263029-1), the Guangxi Natural Science Foundation of China (2023GXNSFAA026434) and the National Natural Science Foundation of China (42474057, 42164001).

Institutional Review Board Statement: Not applicable.

Informed Consent Statement: Not applicable.

Data Availability Statement: The radiosonde data are obtained from the Integrated Global Radiosonde Archive (<http://www1.ncdc.noaa.gov/pub/data/igra/>, accessed on 31 December 2022). GNSS dataset is provided by the GNSS data product service platform of the China Earthquake Administration (www.cgps.ac.cn, accessed on 31 December 2022). The FY-4A PWV data are provided by Fengyun Satellite Remote Sensing Data Service Network (<http://satellite.nsmc.org.cn/>, accessed on 31 December 2022).

Conflicts of Interest: The authors declare no conflict of interest.

References

1. Mendes, V.d.B. Modeling the Neutral-Atmosphere Propagation Delay in Radiometric Space Techniques. Ph.D. Thesis, University of New Brunswick, Fredericton, NB, Canada, 1998.
2. Zhu, H.; Chen, K.; Chai, H.; Ye, Y.; Liu, W. Characterizing extreme drought and wetness in Guangdong, China using global navigation satellite system and precipitation data. *Satell. Navig.* **2024**, *5*, 1. [[CrossRef](#)]
3. Huang, L.; Lu, D.; Chen, F.; Zhang, H.; Zhu, G.; Liu, L. A Deep Learning-Based Approach for Directly Retrieving GNSS Precipitable Water Vapor and Its Application in Typhoon Monitoring. *IEEE Trans. Geosci. Remote Sens.* **2024**, *62*, 4111712. [[CrossRef](#)]
4. Huang, L.; Pan, A.; Chen, F.; Guo, F.; Li, H.; Liu, L. A novel global grid model for soil moisture retrieval considering geographical disparity in spaceborne GNSS-R. *Satell. Navig.* **2024**, *5*, 29. [[CrossRef](#)]
5. Chen, B.; Dai, W.; Liu, Z.; Wu, L.; Xia, P. Assessments of GMI-Derived Precipitable Water Vapor Products over the South and East China Seas Using Radiosonde and GNSS. *Adv. Meteorol.* **2018**, *2018*, 7161328. [[CrossRef](#)]
6. Tsidu, G.M.; Blumenstock, T.; Hase, F. Observations of precipitable water vapour over complex topography of Ethiopia from ground-based GPS, FTIR, radiosonde and ERA-Interim reanalysis. *Atmos. Meas. Tech.* **2015**, *8*, 3277–3295. [[CrossRef](#)]
7. Renju, R.; Raju, C.S.; Mathew, N.; Antony, T.; Moorthy, K.K. Microwave radiometer observations of interannual water vapor variability and vertical structure over a tropical station. *J. Geophys. Res. Atmos.* **2015**, *120*, 4585–4599. [[CrossRef](#)]
8. Mattioli, V.; Westwater, E.R.; Cimini, D.; Liljegren, J.C.; Lesht, B.M.; Gutman, S.I.; Schmidlin, F.J. Analysis of radiosonde and ground-based remotely sensed PWV data from the 2004 North Slope of Alaska Arctic Winter Radiometric Experiment. *J. Atmos. Ocean. Technol.* **2007**, *24*, 415–431. [[CrossRef](#)]
9. Bevis, M.; Businger, S.; Herring, T.A.; Rocken, C.; Anthes, R.A.; Ware, R.H. GPS meteorology: Remote sensing of atmospheric water vapor using the global positioning system. *J. Geophys. Res. Atmos.* **1992**, *97*, 15787–15801. [[CrossRef](#)]
10. Zhang, W.; Lou, Y.; Haase, J.S.; Zhang, R.; Zheng, G.; Huang, J.; Shi, C.; Liu, J. The Use of Ground-Based GPS Precipitable Water Measurements over China to Assess Radiosonde and ERA-Interim Moisture Trends and Errors from 1999 to 2015. *J. Clim.* **2017**, *30*, 7643–7667. [[CrossRef](#)]
11. Mears, C.A.; Wang, J.; Smith, D.; Wentz, F.J. Intercomparison of total precipitable water measurements made by satellite-borne microwave radiometers and ground-based GPS instruments. *J. Geophys. Res. Atmos.* **2015**, *120*, 2492–2504. [[CrossRef](#)]
12. Zhu, G.; Huang, L.; Yang, Y.; Li, J.; Zhou, L.; Liu, L. Refining the ERA5-based global model for vertical adjustment of zenith tropospheric delay. *Satell. Navig.* **2022**, *3*, 27. [[CrossRef](#)]
13. Huang, L.; Liu, Z.; Peng, H.; Xiong, S.; Zhu, G.; Chen, F.; Liu, L.; He, H. A Novel Global Grid Model for Atmospheric Weighted Mean Temperature in Real-Time GNSS Precipitable Water Vapor Sounding. *IEEE J. Sel. Top. Appl. Earth Obs. Remote Sens.* **2023**, *16*, 3322–3335. [[CrossRef](#)]
14. Li, W.; He, Z.; Wu, L.; Liu, S.; Luo, L.; Ye, X.; Gao, H.; Ma, C. Impacts of co-culture of rice and aquatic animals on rice yield and quality: A meta-analysis of field trials. *Field Crops. Res.* **2022**, *280*, 108468. [[CrossRef](#)]
15. Sherwood, S.C.; Roca, R.; Weckwerth, T.M.; Andronova, N.G. Tropospheric water vapor, convection, and climate. *Rev. Geophys.* **2010**, *48*, RG2001. [[CrossRef](#)]
16. Gong, Y.Z.; Liu, Z.Z.; Foster, J.H. Evaluating the Accuracy of Satellite-Based Microwave Radiometer PWV Products Using Shipborne GNSS Observations Across the Pacific Ocean. *IEEE Trans. Geosci. Remote Sens.* **2022**, *60*, 5802210. [[CrossRef](#)]
17. Fujita, M.; Fukuda, T.; Ueki, I.; Moteki, Q.; Ushiyama, T.; Yoneyama, K. Experimental Observations of Precipitable Water Vapor over the Open Ocean Collected by Autonomous Surface Vehicles for Real-Time Monitoring Applications. *Sola* **2020**, *16A*, 19–24. [[CrossRef](#)]
18. Sam Khaniani, A.; Nikraftar, Z.; Zakeri, S. Evaluation of MODIS Near-IR water vapor product over Iran using ground-based GPS measurements. *Atmos. Res.* **2020**, *231*, 104657. [[CrossRef](#)]
19. Wang, Y.; Yang, K.; Pan, Z.Y.; Qin, J.; Chen, D.L.; Lin, C.G.; Chen, Y.Y.; Lazhu; Tang, W.J.; Han, M.L.; et al. Evaluation of Precipitable Water Vapor from Four Satellite Products and Four Reanalysis Datasets against GPS Measurements on the Southern Tibetan Plateau. *J. Clim.* **2017**, *30*, 5699–5713. [[CrossRef](#)]
20. Ma, X.; Yao, Y.; Zhang, B.; Du, Z. FY-3A/MERSI precipitable water vapor reconstruction and calibration using multi-source observation data based on a generalized regression neural network. *Atmos. Res.* **2022**, *265*, 105893. [[CrossRef](#)]
21. Xia, X.; Fu, D.; Shao, W.; Jiang, R.; Wu, S.; Zhang, P.; Yang, D.; Xia, X. Retrieving Precipitable Water Vapor Over Land From Satellite Passive Microwave Radiometer Measurements Using Automated Machine Learning. *Geophys. Res. Lett.* **2023**, *50*, e2023GL105197. [[CrossRef](#)]
22. Wang, G.; Wang, K.F.; Han, W.; Wang, D.Y.; Qiu, X.X. Typhoon Maria Precipitation Retrieval and Evolution Based on the Infrared Brightness Temperature of the Feng-Yun 4A/Advanced Geosynchronous Radiation Imager. *Adv. Meteorol.* **2020**, *2020*, 4245037. [[CrossRef](#)]
23. Wang, X.; Min, M.; Wang, F.; Guo, J.P.; Li, B.; Tang, S.H. Intercomparisons of Cloud Mask Products Among Fengyun-4A, Himawari-8, and MODIS. *IEEE Trans. Geosci. Remote Sens.* **2019**, *57*, 8827–8839. [[CrossRef](#)]

24. Zhu, J.; Shu, J.; Guo, W. Biases Characteristics Assessment of the Advanced Geosynchronous Radiation Imager (AGRI) Measurement on Board Fengyun-4A Geostationary Satellite. *Remote Sens.* **2020**, *12*, 2871. [[CrossRef](#)]
25. Yang, J.; Zhang, Z.; Wei, C.; Lu, F.; Guo, Q. Introducing the New Generation of Chinese Geostationary Weather Satellites, Fengyun-4. *Bull. Am. Meteorol. Soc.* **2017**, *98*, 1637–1658. [[CrossRef](#)]
26. Zhang, Y.; Li, Z.; Li, J. A Preliminary Layer Perceptible Water Vapor Retrieval Algorithm for Fengyun-4 Advanced Geosynchronous Radiation Imager. In Proceedings of the IGARSS 2019—2019 IEEE International Geoscience and Remote Sensing Symposium, Yokohama, Japan, 28 July–2 August 2019; pp. 7564–7566. [[CrossRef](#)]
27. Wang, Y.; Liu, H.; Zhang, Y.; Duan, M.; Tang, S.; Deng, X.J.A.R. Validation of FY-4A AGRI layer precipitable water products using radiosonde data. *Atmos. Res.* **2021**, *253*, 105502. [[CrossRef](#)]
28. Tan, J.; Chen, B.; Wang, W.; Yu, W.; Dai, W. Evaluating Precipitable Water Vapor Products From Fengyun-4A Meteorological Satellite Using Radiosonde, GNSS, and ERA5 Data. *IEEE Trans. Geosci. Remote Sens.* **2022**, *60*, 4106512. [[CrossRef](#)]
29. Zhou, Y.; Wang, X.Z.; Xu, C. Comprehensive evaluation of the precipitable water vapor products of Fengyun satellites via GNSS data over mainland China. *Atmos. Res.* **2024**, *300*, 107235. [[CrossRef](#)]
30. Liu, X.; Wang, Y.; Huang, J.; Yu, T.L.; Jiang, N.H.; Yang, J.; Zhan, W. Assessment and calibration of FY-4A AGRI total precipitable water products based on CMONOC. *Atmos. Res.* **2022**, *271*, 106096. [[CrossRef](#)]
31. Wu, M.L.; Jin, S.G.; Li, Z.C.; Cao, Y.C.; Ping, F.; Tang, X. High-Precision GNSS PWV and Its Variation Characteristics in China Based on Individual Station Meteorological Data. *Remote Sens.* **2021**, *13*, 1296. [[CrossRef](#)]
32. Huang, L.; Mo, Z.; Xie, S.; Liu, L.; Chen, J.; Kang, C.; Wang, S. Spatiotemporal characteristics of GNSS-derived precipitable water vapor during heavy rainfall events in Guilin, China. *Satell. Navig.* **2021**, *2*, 13. [[CrossRef](#)]
33. Nzelibe, I.U.; Tata, H.; Idowu, T.O. Assessment of GNSS zenith tropospheric delay responses to atmospheric variables derived from ERA5 data over Nigeria. *Satell. Navig.* **2023**, *4*, 15. [[CrossRef](#)]
34. Saastamoinen, J. Atmospheric Correction for the Troposphere and Stratosphere in Radio Ranging Satellites. *Use Artif. Satell. Geod.* **1972**, *15*, 247–251. [[CrossRef](#)]
35. Askne, J.; Nordius, H. Estimation of tropospheric delay for microwaves from surface weather data. *Radio Sci.* **1987**, *22*, 379–386. [[CrossRef](#)]
36. Huang, L.K.; Jiang, W.P.; Liu, L.L.; Chen, H.; Ye, S.R. A new global grid model for the determination of atmospheric weighted mean temperature in GPS precipitable water vapor. *J. Geod.* **2019**, *93*, 159–176. [[CrossRef](#)]
37. Huang, L.K.; Liu, L.L.; Chen, H.; Jiang, W.P. An improved atmospheric weighted mean temperature model and its impact on GNSS precipitable water vapor estimates for China. *GPS Solut.* **2019**, *23*, 51. [[CrossRef](#)]
38. Huang, L.; Wang, Y.; Bi, H.; Zhu, G.; Liu, L.; Jiang, W. Initial results of atmospheric weighted mean temperature estimation with Pangu-Weather in real-time GNSS PWV retrieval for China. *GPS Solut.* **2025**, *29*, 48. [[CrossRef](#)]
39. Huang, L.K.; Wang, X.; Xiong, S.; Li, J.Y.; Liu, L.L.; Mo, Z.X.; Fu, B.L.; He, H.C. High-precision GNSS PWV retrieval using dense GNSS sites and in-situ meteorological observations for the evaluation of MERRA-2 and ERA5 reanalysis products over China. *Atmos. Res.* **2022**, *276*, 106247. [[CrossRef](#)]
40. Zhu, G.; Huang, L.K.; Liu, L.L.; Li, C.; Li, J.Y.; Huang, L.; Zhou, L.; He, H.C. A New Approach for the Development of Grid Models Calculating Tropospheric Key Parameters over China. *Remote Sens.* **2021**, *13*, 3546. [[CrossRef](#)]
41. Wang, J.; Zhang, L.; Dai, A. Global estimates of water-vapor-weighted mean temperature of the atmosphere for GPS applications. *J. Geophys. Res. Atmos.* **2005**, *110*, D21101. [[CrossRef](#)]
42. Shikhovtsev, A.Y.; Kovadlo, P.G.; Khaikin, V.B.; Kiselev, A.V. Precipitable Water Vapor and Fractional Clear Sky Statistics within the Big Telescope Alt-Azimuthal Region. *Remote Sens.* **2022**, *14*, 6221. [[CrossRef](#)]
43. Birkenheuer, D.; Gutman, S. A Comparison of GOES Moisture-Derived Product and GPS-IPW Data during IHOP-2002. *J. Atmos. Ocean. Technol.* **2005**, *22*, 1838–1845. [[CrossRef](#)]
44. Schmit, T.J.; Feltz, W.F.; Menzel, W.P.; Jung, J.; Noel, A.P.; Heil, J.N.; Nelson, J.P.; Wade, G.S. Validation and Use of GOES Sounder Moisture Information. *Weather Forecast.* **2002**, *17*, 139–154. [[CrossRef](#)]
45. Zhang, H.; Yuan, Y.; Li, W.; Zhang, B. A Real-Time Precipitable Water Vapor Monitoring System Using the National GNSS Network of China: Method and Preliminary Results. *IEEE J. Sel. Top. Appl. Earth Obs. Remote Sens.* **2019**, *12*, 1587–1598. [[CrossRef](#)]
46. Zhao, Q.; Yao, Y.; Yao, W.; Zhang, S. GNSS-derived PWV and comparison with radiosonde and ECMWF ERA-Interim data over mainland China. *J. Atmos. Sol.-Terr. Phys.* **2019**, *182*, 85–92. [[CrossRef](#)]
47. Zhao, Q.; Yang, P.; Yao, W.; Yao, Y. Hourly PWV Dataset Derived from GNSS Observations in China. *Sensors* **2020**, *20*, 231. [[CrossRef](#)]
48. Shi, C.; Zhou, L.H.; Fan, L.; Zhang, W.X.; Cao, Y.C.; Wang, C.; Xiao, F.; Lü, G.Q.; Liang, H. Analysis of “21.7” extreme rainstorm process in Henan Province using BeiDou/GNSS observation. *Chin. J. Geophys. Chin. Ed.* **2022**, *65*, 186–196. [[CrossRef](#)]
49. Khaikin, V.B.; Shikhovtsev, A.Y.; Mironov, A.P. Statistical Characteristics of Precipitated Water Vapor, Optical Depth and Cloudiness in the Northern Part of Russia. *Astron. Rep.* **2024**, *68*, 222–232. [[CrossRef](#)]

50. Bai, J.N.; Lou, Y.D.; Zhang, W.X.; Zhou, Y.Z.; Zhang, Z.Y.; Shi, C. Assessment and calibration of MODIS precipitable water vapor products based on GPS network over China. *Atmos. Res.* **2021**, *254*, 105504. [[CrossRef](#)]
51. Gui, K.; Che, H.Z.; Chen, Q.L.; Zeng, Z.L.; Liu, H.Z.; Wang, Y.Q.; Zheng, Y.; Sun, T.Z.; Liao, T.T.; Wang, H.; et al. Evaluation of radiosonde, MODIS-NIR-Clear, and AERONET precipitable water vapor using IGS ground-based GPS measurements over China. *Atmos. Res.* **2017**, *197*, 461–473. [[CrossRef](#)]
52. Wang, H.; He, J.X.; Wei, M.; Zhang, Z.D. Synthesis Analysis of One Severe Convection Precipitation Event in Jiangsu Using Ground-Based GPS Technology. *Atmosphere* **2015**, *6*, 908–927. [[CrossRef](#)]
53. Iwabuchi, T.; Naito, I.; Mannoji, N. A comparison of Global Positioning System retrieved precipitable water vapor with the numerical weather prediction analysis data over the Japanese Islands. *J. Geophys. Res. Atmos.* **2000**, *105*, 4573–4585. [[CrossRef](#)]
54. Pérez-Jordán, G.; Castro-Almazán, J.A.; Muñoz-Tuñón, C.; Codina, B.; Vernin, J. Forecasting the precipitable water vapour content: Validation for astronomical observatories using radiosoundings. *Mon. Not. R. Astron. Soc.* **2015**, *452*, 1992–2003. [[CrossRef](#)]
55. Li, Z.H.; Fielding, E.J.; Cross, P. Integration of InSAR Time-Series Analysis and Water-Vapor Correction for Mapping Postseismic Motion After the 2003 Bam (Iran) Earthquake. *IEEE Trans. Geosci. Remote Sens.* **2009**, *47*, 3220–3230. [[CrossRef](#)]
56. Mateus, P.; Tomé, R.; Nico, G.; Catalao, J. Three-Dimensional Variational Assimilation of InSAR PWV Using the WRFDA Model. *IEEE Trans. Geosci. Remote Sens.* **2016**, *54*, 7323–7330. [[CrossRef](#)]

Disclaimer/Publisher’s Note: The statements, opinions and data contained in all publications are solely those of the individual author(s) and contributor(s) and not of MDPI and/or the editor(s). MDPI and/or the editor(s) disclaim responsibility for any injury to people or property resulting from any ideas, methods, instructions or products referred to in the content.